

Ab Initio Molecular Dynamics Study of the Proton Transfer in Hydroxyl Ion-Induced Hydrolysis of Aluminum Monomers

Longfei Guo, Yuguo Xia,* Xiuling Jiao,* and Dairong Chen



Cite This: *J. Phys. Chem. B* 2023, 127, 7342–7351



Read Online

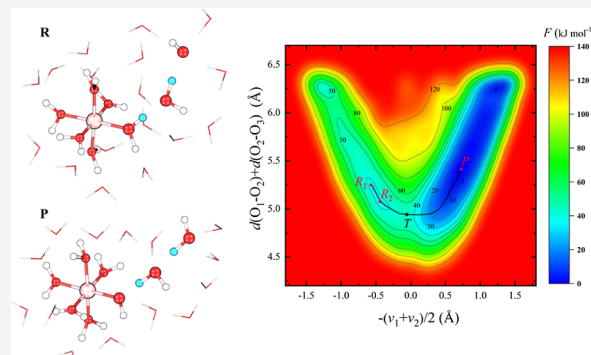
ACCESS |

Metrics & More

Article Recommendations

Supporting Information

ABSTRACT: The hydrolysis process of $\text{Al}(\text{H}_2\text{O})_6^{3+}$ induced by hydroxyl ions (OH^-) is significant to aluminum solution chemistry. Previous investigations of hydrolysis reactions have primarily relied on static calculations in an implicit solvent environment. Herein, we employ ab initio molecular dynamics (AIMD) to investigate the evolution process of $\text{Al}(\text{H}_2\text{O})_6^{3+}$ under various local alkaline conditions in an explicit solvent environment. Our work demonstrates the effect of solvent water in hydrolysis reactions. Specifically, the stepwise hydrolysis reaction induced by hydroxyl ions involves water wire compression and concerted proton transfers. Dehydration reactions occur when the number of hydroxyl ligands attached to the aluminum ion (Al^{3+}) equals or exceeds three. Moreover, the $\text{Al}(\text{H}_2\text{O})_n(\text{OH})_3$ species exhibit unique hydrolysis and dehydration reaction characteristics compared to other species. The geometrically stable aluminum monomers determined by AIMD are $\text{Al}(\text{H}_2\text{O})_5(\text{OH})_1^{2+}$, $\text{Al}(\text{H}_2\text{O})_4(\text{OH})_2^+$, $\text{Al}(\text{H}_2\text{O})_1(\text{OH})_3$, and $\text{Al}(\text{OH})_4^-$. In addition, the topological analysis analyzes the interaction between Al^{3+} and coordinated H_2O in different configurations, indicating the weakest interaction appearing in $\text{Al}(\text{H}_2\text{O})_n(\text{OH})_3$ species.



1. INTRODUCTION

Aluminum, the third most abundant element in the earth's crust after oxygen and silicon, is widely used in modern society for its excellent performance and low cost. Aluminum compounds, such as alumina, aluminum hydroxide, and aluminum sulfate, find diverse applications in electronic devices, heat insulation, and water treatment.^{1–5} The sol–gel method is widely employed for the preparation of various aluminum products due to its simplicity, economic applicability, and wide range of applications.^{6–10} Nanoscale aluminum particles gradually form through hydrolysis and polymerization reactions during the sol process. Despite numerous studies conducted on large polymeric species that exist stably in solution, such as $\text{AlO}_4\text{Al}_{12}(\text{OH})_{24}(\text{H}_2\text{O})_{12}^{7+}$ and $\text{Al}_{30}\text{O}_8(\text{OH})_{56}(\text{H}_2\text{O})_{24}^{18+}$, the mechanisms behind the formation and growth of these aluminum clusters remain unclear.^{11–14} Since aluminum oligomers are the basis for the formation of polymeric species, the study of aluminum oligomers, particularly the most fundamental aluminum monomers, contributes to revealing the formation process of polynuclear aluminum clusters and provides guidance for the preparation of aluminum-based materials.^{15–18}

In an aqueous solution, Al^{3+} forms a solvent shell structure like other ions (Zn^{2+} and Fe^{2+}) with a hexahydrate complex $\text{Al}(\text{H}_2\text{O})_6^{3+}$,^{19–21} that is, the central Al^{3+} ion is coordinated with six water molecules by the Al–O ligand bonds. Due to the electrons of coordinated water molecules tending to be drawn toward the positively charged aluminum ion, the coordination-

induced bond weakening phenomenon appears in O–H covalent bonds,²² making the aluminum monomer $\text{Al}(\text{H}_2\text{O})_6^{3+}$ prone to hydrolyze, particularly induced by the hydroxyl ions in base titration. Besides, the dehydration reactions simultaneously take place along with the hydrolysis process, leading to the formation of a variety of hydrolysis products ($\text{Al}(\text{H}_2\text{O})_n(\text{OH})_m^{3-m}$). However, the coexistence of multiple aluminum species in solution often causes disturbances in experimental observation, rendering detailed research of the hydrolysis and dehydration reaction processes and identifying different intermediate hydrolytic species quite challenging. In contrast to the difficulties in experimental characterizations, computational studies conducted at the atomic level have gained momentum in recent years.^{23–26} Density functional theory-based static calculations have been employed to study aluminum monomers' hydrolysis and dehydration reactions, albeit with limited water molecules and lacking a complete solvent environment. Furthermore, the specific configurations applied in static calculation models have been constructed artificially, making it difficult to obtain all reaction paths and

Received: April 28, 2023

Revised: July 13, 2023

Published: August 9, 2023



complete energy landscapes. Therefore, exploring aluminum monomers' hydrolysis and dehydration reactions in the presence of explicit solvent water molecules is of great importance.

Herein, we employ AIMD to investigate the forced hydrolysis reactions of aluminum monomers induced by external hydroxyl ions under an explicit solvent model.²⁷ In contrast to previous static calculation studies involving small systems with minimal water molecules, our work expands the scope by including a larger amount of water and varying numbers of hydroxyl ions, allowing us to investigate the hydrolysis reactions of aluminum monomers under different local alkaline conditions. The explicit solvent model enables the feasibility of directly observing the entire proton transfer (PT) process and the solvent structure around the aluminum monomer. Meanwhile, we have also demonstrated the concerted PT involved in the hydrolysis of aluminum monomers by generating sufficient AIMD samples. Besides, we also explore the free energy surface of typical concerted PT events by the metadynamics approach. Meanwhile, the electronic structures and stability of various $\text{Al}(\text{H}_2\text{O})_n(\text{OH})_{m-3}^+$ species are discussed in detail.

2. COMPUTATIONAL SECTIONS

2.1. Computational Methods. The AIMD simulations were carried out using the Quickstep module of the CP2K7.1 package.^{28,29} The Becke–Lee–Yang–Parr (BLYP)^{30,31} density functional corrected by the empirical dispersion corrections of Grimme's D3 was employed,³² which has been widely used in previous studies of aluminum in aqueous environments.^{33–35} To accurately depict the potential near nuclei, Goedecker–Teter–Hutter (GTH) pseudopotentials were employed.³⁶ A mixed Gaussian and plane wave (PW) approach was taken,³⁷ where double- ζ valence augmented with polarization Gaussian basis sets were adopted,³⁸ and the PW expansion of the charge density with a cutoff energy of 300 Ry was used. The target accuracy for the self-consistent field method's convergence was set at 10^{-6} au. Besides, the AIMD simulations were performed in a canonical ensemble (NVT) at 330 K with a Nose–Hoover thermostat to regulate the temperature.^{39,40} The time step for the motion of nuclei in AIMD was 0.5 fs.

2.2. Model Setup and Details for AIMD Simulation. The initial structure consisted of 1 $\text{Al}(\text{H}_2\text{O})_6^{3+}$ and 130 H_2O molecules, totaling 409 atoms, and was enclosed in a three-dimensional box with periodic boundary conditions (Figure S1). The cubic box size was $16 \times 16 \times 16 \text{ \AA}^3$ with a density of approximately 1 g cm^{-3} . The net charge of the system was +3, and a compensating jellium background was included to avoid divergence. A 5 ps pre-equilibrium AIMD simulation was first performed for the initial structure, followed by an equilibrium simulation of 20 ps. To determine the distribution of water molecules around Al^{3+} , the radial distribution function (RDF) of Al–O and the combined distribution function (CDF) of Al–O distance and Al–O–H angle were obtained from the 20 ps equilibrium simulation trajectory with the TRAVIS software.⁴¹ To investigate the hydrolysis process of $\text{Al}(\text{H}_2\text{O})_6^{3+}$ induced by hydroxyl ions under different local alkaline conditions, aluminum monomers with different numbers (1, 2, 3, and 4) of hydroxyl ions were produced by replacing the corresponding number of H_2O molecules from the structure at the 10th ps in the 20 ps equilibrium simulation trajectory. Each geometry was pre-equilibrated for at least 3 ps to ensure the rationality of the solvation structures.⁴² Four individual AIMD

simulations were then restarted from the end of each pre-equilibrium simulation. Every AIMD simulation continued until all hydroxyl ions in the solvent had participated in hydrolysis reactions, and eventually, the number of OH ligands in the final product $\text{Al}(\text{H}_2\text{O})_n(\text{OH})_{m-3}^+$ was equal to the number of hydroxyl ions in the original reactant solution. The same operations were carried out for the structures at 15th and 20th ps, resulting in twelve AIMD trajectories to illustrate aluminum monomer hydrolysis and dehydration reactions under different local alkaline conditions. The more hydroxyl ions were contained in the system, the corresponding notional pH is higher. Three AIMD trajectories for $\text{Al}(\text{H}_2\text{O})_6^{3+}$ with the same number of hydroxyl ions but with different initial structures ensured the adequacy of the sampling number. Notably, we proceeded to conduct no less than a 25 ps AIMD simulation for each ending product after achieving an equilibrium state to explore their stability.

2.3. Well-Tempered Metadynamics. The hydrolysis reaction of $\text{Al}(\text{H}_2\text{O})_6^{3+}$ induced by one hydroxyl ion was taken as an example to perform well-tempered metadynamics to investigate the free-energy profile of the double jump mode PT,^{43,44} which was calculated with the PLUMED 2.9.0 program.⁴⁵ Two collective variables (CVs) were introduced to describe the double jump mode PT, where CV_1 was defined as $-(v_1 + v_2)/2$, $v_1 = d(\text{O}_1-\text{H}_1) - d(\text{O}_2-\text{H}_1)$, and $v_2 = d(\text{O}_2-\text{H}_2) - d(\text{O}_3-\text{H}_2)$ and CV_2 was defined as $d(\text{O}_1-\text{O}_2) + d(\text{O}_2-\text{O}_3)$.⁴² Among others, CV_1 changed from a negative value to a positive value, indicating that the reaction occurred, and CV_2 represented the water-wire distance between Al^{3+} and OH^- . The deposition rate for the Gaussian hills was 20 MD steps, with Gaussian widths for CV_1 and CV_2 set to 0.12 and 0.1 Å, respectively. The initial Gaussian height was 3 kJ mol⁻¹, and the bias factor was 12. Besides, some wall restraints were implemented to ensure a rational structure in metadynamics, and the details of wall settings are supplemented in the Supporting Information. The well-tempered metadynamics result was analyzed with the metadynminer packages.⁴⁶

2.4. Static Calculations and Topological Analysis. All static calculations were conducted using Gaussian 09.⁴⁷ Nine configurations that appeared in AIMD simulations were used to perform the electron density topological analysis. The initial structures employed the gas-phase supermolecule (GP-SM) clusters in a previous report.²⁶ In the GP-SM model, 12, 13, and 14 explicit solvent water molecules were added for the hexa-, penta-, and tetra-coordinated configurations, respectively. The polarizable continuum model (PCM) in the integral equation formalism variant (IEFPCM)⁴⁸ was used to represent the effect of the remaining solvent. Geometry optimizations and frequency calculations were carried out at the B3LYP/def2-TZVP level with a D3 empirical dispersion correction. No imaginary frequency appeared in vibrational frequency analyses after geometry optimizations, indicating that stable conformations were achieved.

The condensed-to-atom electrophilicity index (ω^+) of hydrogen atoms in coordinated water of Al^{3+} was calculated to measure reactivity in nucleophilic attack during PT events. The interaction of O_w (the O atoms in coordinated water) with Al^{3+} was investigated by the topological analysis of the electron density based on the quantum theory of atoms in molecules.⁴⁹ The nature of the Al– O_w ligand bond was characterized by a series of descriptors of the electron density at the bond critical points (BCPs). The bonding degree of Al– O_w was also reflected by Mayer bond order values.⁵⁰ The

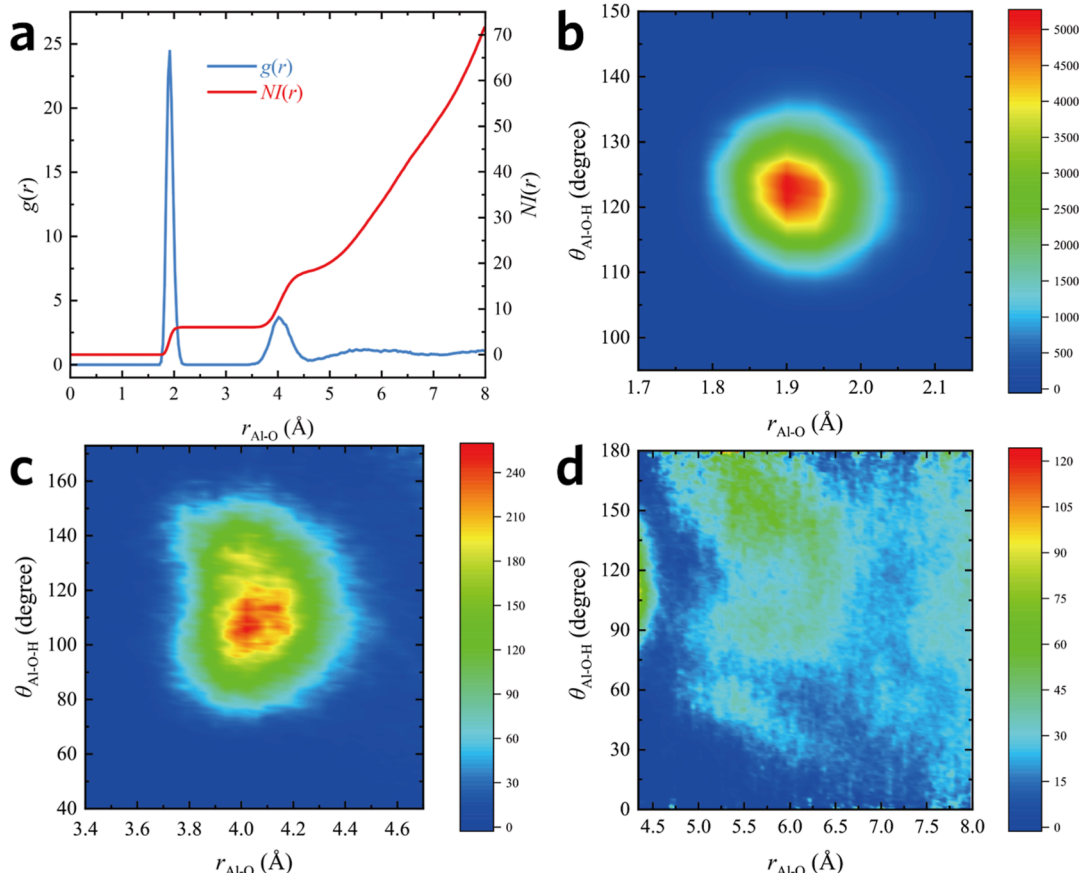


Figure 1. (a) RDF for Al–O pairs. CDF of Al–O distance and Al–O–H angle at (b) 1.7–2.1, (c) 3.4–4.7, and (d) 4.35–8.0 Å.

condensed-to-atom electrophilicity index, topological analysis descriptors, and Mayer bond order values were obtained using Multiwfn software.⁵¹

3. RESULTS AND DISCUSSION

3.1. Solvent Water Shell Structure Surrounding Al^{3+} . In order to clarify the solvent structure around Al^{3+} and reasonably build the initial structures of AIMD of hydroxyl ion-induced hydrolysis reactions, RDF and CDF results are discussed first. Figure 1a displays two distinct peaks observed in the RDF $g_{\text{Al}-\text{O}}(r)$, indicating the presence of the first and second hydrated water shell layers of Al^{3+} . Specifically, the first peak is located at 1.92 Å and the second peak at 4.02 Å in $g_{\text{Al}-\text{O}}(r)$. A previous computational study showed two peaks at 1.92 and 4.09 Å, respectively.²¹ A theoretical model obtained on the basis of experimental X-ray diffraction data showed two peaks at 2.07 and 4.05 Å, respectively, when the concentration of Al^{3+} was 0.68 mol L⁻¹.⁵² Our results of RDF are basically consistent with the above research. To gain further insight into the solvent water distribution at different Al–O distances, the CDF was plotted at various Al–O distances, as shown in Figure 1b–d. Figure 1b,c presents the angular distribution features of the first and second water layers, respectively. Notably, the angular distribution of the first water layer is highly concentrated in the range of 117–127°, while the second water layer is centrally distributed at 98–120°. Thus, Al^{3+} has apparently regularly distributed two water layers, but the second layer is not as regularly distributed as the first layer. The characteristics of the water molecule distribution beyond the second layer are depicted in Figure 1d. Interestingly,

although the RDF diagram does not display a discernible third layer of water, the CDF reveals that a region of high concentration arises at the coordinates (4.6 Å, 150°), where the oxygen atoms are oriented toward the Al^{3+} ion and the hydrogen atoms deviate from it. Although the arrangement of water molecules beyond the second layer is not as regular as the preceding two layers, it is evident that the effect of aluminum ions on the solvent water distribution extends beyond two hydration layers. To ensure the authenticity of the solvent structure in the initial structures in the next AIMD simulations of the hydroxyl ion-induced hydrolysis, the initial locations of hydroxyl ions were all positioned more than 7.5 Å away from Al^{3+} to prevent OH^- from initially appearing in regions occupied by regularly distributed water molecules.

3.2. PT during Hydroxyl Ion-Induced Hydrolysis Reactions. Based on the twelve AIMD trajectories, we summarize the characteristics of the hydroxyl ion-induced hydrolysis reactions at different notional pHs. On the whole, the hydroxyl ion-induced hydrolysis of aluminum monomers occurs in two stages. The first stage involves the transfer of hydroxyl ions in bulk water, while in the second stage, hydroxyl ions approach $\text{Al}(\text{H}_2\text{O})_n(\text{OH})_m{}^{3-m}$ at a contact distance, characterized by two types: direct hydrogen bonding (H-bond) between OH^- and $\text{Al}(\text{H}_2\text{O})_n(\text{OH})_m{}^{3-m}$ or through one or two intermediate water molecules forming a water line connected by H-bonds. During the second stage, protons transfer from the first coordination layer water of Al^{3+} to OH^- . Most PT events in the second stage occur in a concerted proton hopping way involving the simultaneous jumping of two or three protons.^{53,54} The $\text{Al}(\text{H}_2\text{O})_n(\text{OH})_m{}^{3-m}$ loses a proton after a

PT event and converts to $\text{Al}(\text{H}_2\text{O})_{n-1}(\text{OH})_{m+1}^{2-m}$, while the OH^- acquires a proton and converts to H_2O . The reactions observed in AIMD simulations, including forced hydrolysis reactions in eqs 1–4, dehydration reactions in eqs 5 and 6, and hydration reactions in eq 7, are all listed in Table 1.

Table 1. Hydrolysis, Dehydration, and Hydration Reactions Appeared in the AIMD Simulations

ID	reaction equations
1	$\text{Al}(\text{H}_2\text{O})_6^{3+} + \text{OH}^- \rightarrow \text{Al}(\text{H}_2\text{O})_5(\text{OH})_1^{2+} + \text{H}_2\text{O}$
2	$\text{Al}(\text{H}_2\text{O})_5(\text{OH})_1^{2+} + \text{OH}^- \rightarrow \text{Al}(\text{H}_2\text{O})_4(\text{OH})_2^+ + \text{H}_2\text{O}$
3	$\text{Al}(\text{H}_2\text{O})_4(\text{OH})_2^+ + \text{OH}^- \rightarrow \text{Al}(\text{H}_2\text{O})_3(\text{OH})_3 + \text{H}_2\text{O}$
4a	$\text{Al}(\text{H}_2\text{O})_1(\text{OH})_3 + \text{OH}^- \rightarrow \text{Al}(\text{OH})_4^- + \text{H}_2\text{O}$
4b	$\text{Al}(\text{H}_2\text{O})_2(\text{OH})_3 + \text{OH}^- \rightarrow \text{Al}(\text{H}_2\text{O})_1(\text{OH})_4^- + \text{H}_2\text{O}$
4c	$\text{Al}(\text{H}_2\text{O})_3(\text{OH})_3 + \text{OH}^- \rightarrow \text{Al}(\text{H}_2\text{O})_2(\text{OH})_4^- + \text{H}_2\text{O}$
5a	$\text{Al}(\text{H}_2\text{O})_3(\text{OH})_3 \rightarrow \text{Al}(\text{H}_2\text{O})_2(\text{OH})_3 + \text{H}_2\text{O}$
5b	$\text{Al}(\text{H}_2\text{O})_2(\text{OH})_3 \rightarrow \text{Al}(\text{H}_2\text{O})_1(\text{OH})_3 + \text{H}_2\text{O}$
6a	$\text{Al}(\text{H}_2\text{O})_2(\text{OH})_4^- \rightarrow \text{Al}(\text{H}_2\text{O})_1(\text{OH})_4^- + \text{H}_2\text{O}$
6b	$\text{Al}(\text{H}_2\text{O})_1(\text{OH})_4^- \rightarrow \text{Al}(\text{OH})_4^- + \text{H}_2\text{O}$
7	$\text{Al}(\text{H}_2\text{O})_1(\text{OH})_3 + \text{H}_2\text{O} \rightarrow \text{mer-Al}(\text{H}_2\text{O})_2(\text{OH})_3$

3.2.1. First Stage: Hydroxyl Ions Transfer in Bulk Water. Herein, we investigated the solvation structure of hydroxyl ions and their transfer in water. Consistent with prior research,^{55–57} the aqueous solution was found to contain two distinct solvation structures of the hydroxyl ion, namely, three-coordination and hypercoordination, with the latter being the more abundant. Generally, the three-coordination structure was determined to be more energetically favorable than the hypercoordination structure for PT.⁴² Through at least 3 ps of pre-equilibrium AIMD simulations, it was observed that nearly all hydroxyl ions in solution existed in the hypercoordination structure, which corresponds with the findings of a recent study.⁴² Besides, the transfer of hydroxyl ions in water was then characterized by monitoring changes in oxygen atoms in OH^- . Figure 2 illustrates a comprehensive example of OH^- transfer in which additive OH^- moves from solution to aluminum monomer, corresponding to the oxygen atom delivered from a to j (Figure S2). Notably, numerous rattling events occurred during this process, characterized by the rapid transfer of protons back and forth, resulting in spikes. Moreover, the PT behavior during OH^- diffusion exhibited an evident alternation of burst and rest periods. Specifically, 1–2 and 3–4 ps were identified as burst periods, in which the motion of OH^- spans two or three water molecules on the subpicosecond timescale. Conversely, 0–1, 2–3, and 4–13 ps constituted the rest period where no long-range migration of the proton occurred during the OH^- diffusion process. Finally, the external OH^- fully transferred into the aluminum monomer and existed as an OH ligand to Al^{3+} after 13 ps.

3.2.2. Second Stage: PT within Contact Distance. When multiple hydroxyl ions are present in the solution, the PT reaction between $\text{Al}(\text{H}_2\text{O})_n(\text{OH})_m^{3-m}$ and OH^- within contact distance occurs independently, and no simultaneous hydrolysis reactions of eqs 1–4 are observed. Three PT pathways exist within the contact distance. As depicted in Figure 3a, in the first case, OH^- links with $\text{Al}(\text{H}_2\text{O})_n(\text{OH})_m^{3-m}$

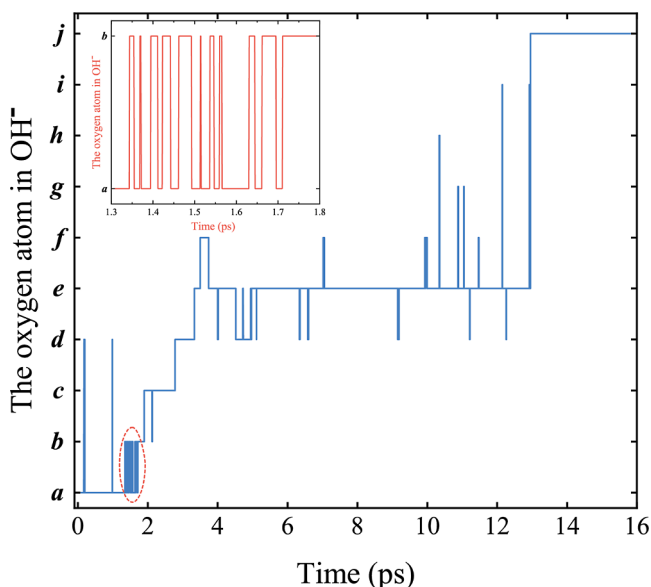


Figure 2. Evolution of oxygen atoms in hydroxyl ions versus time. The labels a–j in the vertical axis represent different oxygen atoms in OH^- . The inset image corresponds to the events in 1.3–1.8 ps.

by one water molecule, and two protons jump almost simultaneously, which is recognized as the “double jump” mode. In the second case, there are two linked middle water molecules between OH^- and $\text{Al}(\text{H}_2\text{O})_n(\text{OH})_m^{3-m}$, and three protons jump all at once (Figure 3b), which is referred to as the “triple jump” mode. The first two ways resemble the correlated PT events of OH^- diffusion^{42,54} and the recombination of hydronium and hydroxide ions in water,⁵³ in which two or three protons jump at once and typically with collective compression of the water wire. Although what we have studied is the hydrolysis reactions of aluminum monomers, our findings concur with their studies just in terms of the PT mode.

Figure 3d displays the changes of associated O–H distances and the sum of O–O distances in a 1 ps span of AIMD, including a double jump mode PT event, where the $d(\text{O}_2-\text{H}_1)$ and $d(\text{O}_3-\text{H}_2)$ increase concurrently at 0.44 ps, both exceeding 1.24 Å after 0.45 ps. Meanwhile, the sum of O–O distances ($d(\text{O}_2-\text{O}_1) + d(\text{O}_3-\text{O}_2)$) decreases from 0.4 ps and reaches the minimum value at 0.45 ps. Similarly, Figure 3e reveals that the first PT occurs at around 0.3 ps, which is ca. 10 fs ahead of the second, and the second PT occurs about 20 fs ahead of the third. The sum of O–O distances ($d(\text{O}_4-\text{O}_3) + d(\text{O}_3-\text{O}_2) + d(\text{O}_2-\text{O}_1)$) decreases from 0.25 to 0.3 ps. The triple jump mode PT involves the sequential transfer of three protons and tends to take longer than the double jump mode PT but remains within a 50 fs timescale. Notably, a lag time (<50 fs) may appear in some correlated PT events⁵³ because one of the protons transfers before the others. The above descriptions in Figure 3d,e pertain to situations in which the double and triple jump mode PT events occur with collective compression of the water wire. A few exceptions with no obvious collective water wire compression are observed (Figure S3), and they all have longer lag times of more than 40 fs but less than 50 fs. Since the distance between the two oxygen atoms involving the earlier passed proton becomes larger during the lag time, there is no reduction in the sum of O–O distances.

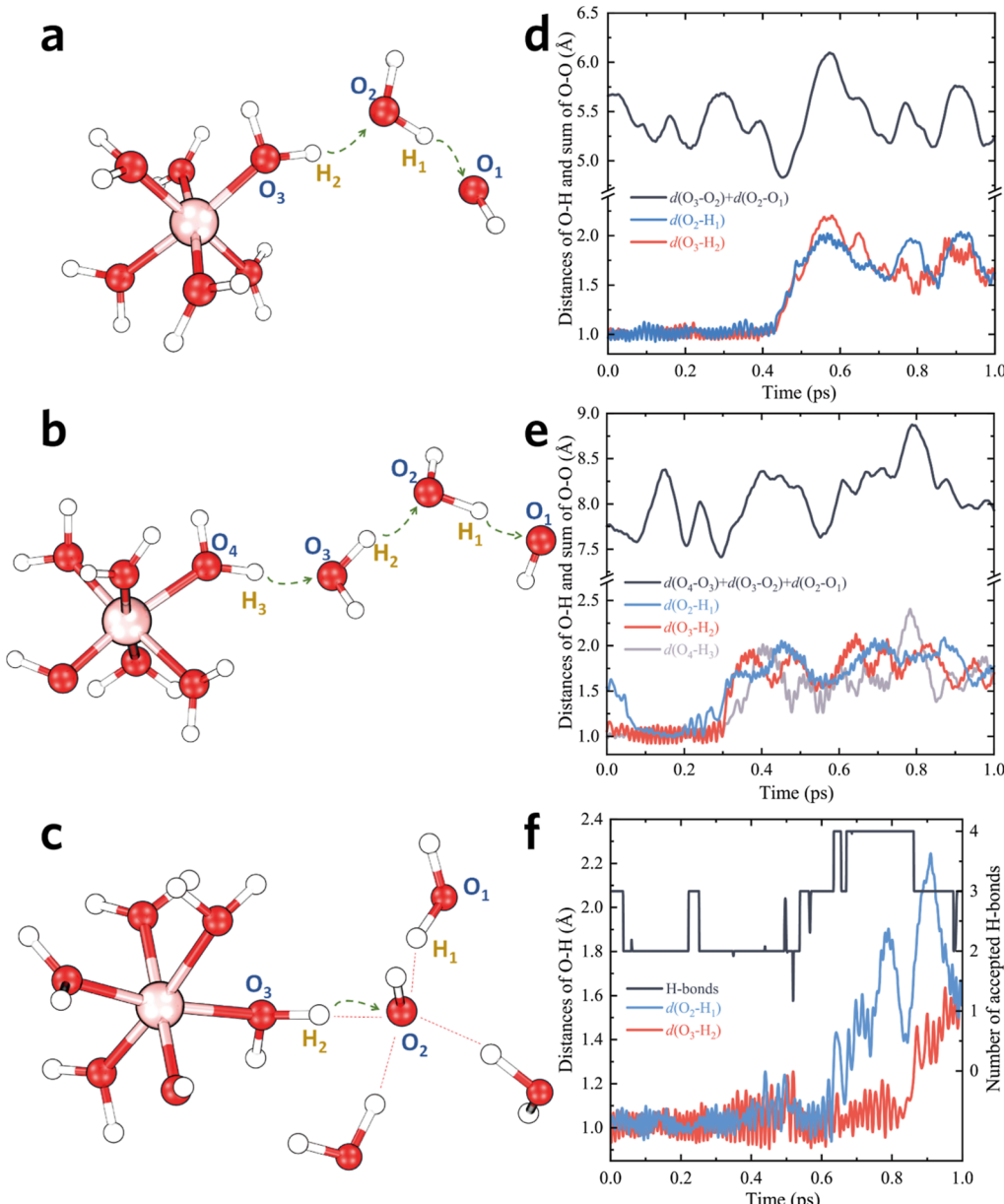


Figure 3. Schematic diagram of three PT ways within contact distance: (a) double jump mode, (b) triple jump mode, and (c) single jump mode. Green dashed lines with arrows in (a–c) represent the PT direction, and red dashed lines in (c) indicate hydrogen bonds. Distance change of O–H and the water wire length with time: (d) double jump mode, (e) triple jump mode, (f) single jump mode. $d(\text{A}-\text{B})$ represents the distance between atoms A and B.

In the third case, no intermediate water molecules exist between OH^- and $\text{Al}(\text{H}_2\text{O})_n(\text{OH})_{m-3}$, and OH^- directly forms a hydrogen bond with the H_2O molecule in the first coordination water layer of Al^{3+} (Figure 3c), which is identified as the “single jump” mode and follows the Grotthuss mechanism. Figure 3f shows the changes of associated O–H distances and the number of accepted H-bonds of OH^- in a 1 ps span of AIMD, including a single jump mode PT event. Specifically, a hydroxide ion (O_2H^-) generates after the H_1 atom departs from the O_2 atom at 0.67 ps and remains for 0.2 ps until the H_2 atom transfers to the O_2 atom at 0.87 ps. The number of H-bond reserves at 4 ranging from 0.67 to 0.87 ps, indicative of the formation of the hypercoordination structure consisting of the hydroxide ion and H-bonds. A recent study suggests that PT events of OH^- in the aqueous solution are strongly hindered by the hypercoordination structure.⁴²

Herein, the formation of the hypercoordination structure allows OH^- to remain stable in contact with the first water layer of Al^{3+} for a period of time, suggesting that the appearance of a single jump mode PT is strongly related to the local solvent structure.

The ratios of the numbers of the three different PT pathways in each hydrolysis reaction under varying notional pH are illustrated in Figure 4a. The total number of each of the three PT pathways is in a ratio of 21:5:4, respectively. Notably, the double jump mode PT predominates in eqs 1–3, regardless of the number of OH^- in the system, while only the single jump mode PT appears in eqs 4b,c. Currently, it is known that PT events in the diffusion of OH^- largely prefer double jump,⁴² while in the recombination of hydronium and hydroxide ions, they prefer triple jump.⁵³ Both jump modes referred to above are concerted PT events with water wire compression, which is

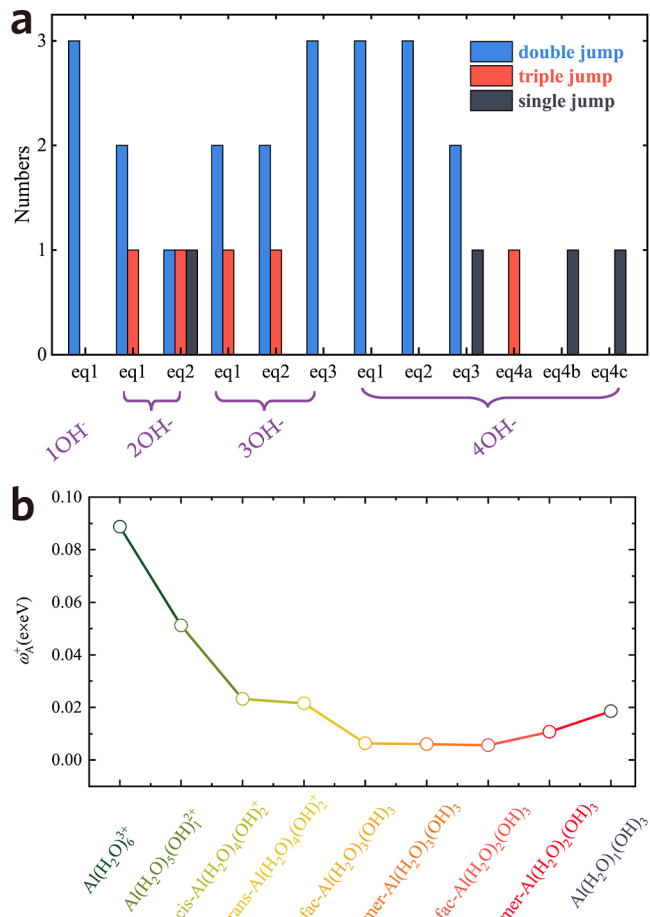


Figure 4. (a) Hydrolysis of the aluminum monomer under varying numbers of hydroxyl ions. (b) Average condensed-to-atom electrophilicity index ($\omega + A$) of hydrogen atoms in coordinated water in different species.

consistent with what we have found in the hydrolysis of aluminum monomers. The PT events prefer a double jump mode in hydrolysis reactions, followed by a triple jump mode. And the occurrence probability of a single jump mode is extremely dependent on specific reactions. We speculate that the effect of Al^{3+} on PT events is twofold: first, it changes the solvent structure, making the distribution of water molecules more orderly and thus stabilizing the water wire, and second, it polarizes the coordinated water, making the hydrogen atoms more active than the bulk water.

Besides, we employed the average condensed-to-atom electrophilicity index ($\omega + A$) of hydrogen atoms to facilitate the comparison of hydrogen atom reactivity in coordinated water of Al^{3+} in different species (Figure 4b and Table S1).^{58,59} Theoretically, the value of $\omega + A$ is negatively correlated with the number of OH ligands. Specifically, the $\omega + A$ values of $\text{Al}(\text{H}_2\text{O})_n(\text{OH})_3$ ($n = 2, 3$) are considerably smaller than those of other species. We speculate that this may be caused by the central Al^{3+} inducing a weaker attractive effect on the electrons in coordinated water as the number of OH ligands increases. Consequently, for $\text{Al}(\text{H}_2\text{O})_n(\text{OH})_3$ ($n = 2, 3$), the electrophilicity of hydrogen atoms in coordinated water becomes the weakest and not reactive enough to initiate collective PT events. However, with the number of water ligands decreasing to 1 in $\text{Al}(\text{H}_2\text{O})_n(\text{OH})_3$, the two hydrogen atoms in the water ligand become more reactive, enabling collective PT events to

occur. Similar results for the change of $\omega + A$ for hydrogen atoms in water ligands were observed in iron monomers.⁶⁰

3.3. Well-Tempered Metadynamics. To further clarify the characteristics of concerted PT events, we obtained the free energy surface by well-tempered metadynamics. Figure 5

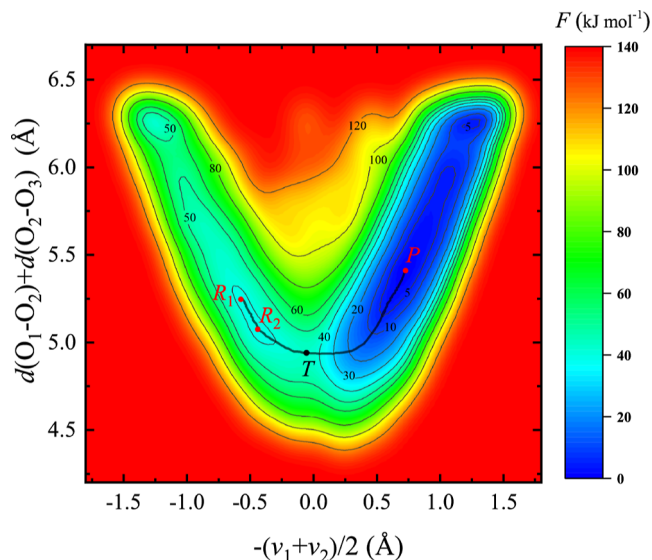


Figure 5. Free energy profile for a double jump mode PT. The atomic labels in Figure 3a are used for CV construction. R_1 , R_2 , and P are local minimum points. The black line connecting R and P is the minimum free energy path. The maximum free energy value in the minimum free energy path is located in point T .

presents the free energy profile of the double jump mode PT in the reaction of $\text{Al}(\text{H}_2\text{O})_6^{3+}$ and OH^- . The reactant state contains two local minimum points, R_1 and R_2 , with corresponding free energy values of 39.66 and 39.36 kJ mol^{-1} , respectively. Given that the differences in free energy are minimal in the region bounded by contour 40 kJ mol^{-1} , where both R_1 and R_2 are located, it can be assumed that the reactant moves easily within this region. The product state is represented by the local minimum point P , with a free energy value of 0 kJ mol^{-1} . The transition state represented by point T possesses a free energy value of 43.51 kJ mol^{-1} . The reaction easily proceeds because the free energy of the product is approximately 40 kJ mol^{-1} lower than that of the reactant, and the free energy barrier is only ca. 4 kJ mol^{-1} . The double jump mode PT involves collective compression of the water wire between $\text{Al}(\text{H}_2\text{O})_6^{3+}$ and OH^- , as evidenced by the minimum free energy path. In comparison with the free energy landscape of double PT via hydroxide in water,⁴² the inducing effect of Al^{3+} on ligand water alters the free energy surface of the double proton jump. Specifically, the free energy barrier becomes extremely low, facilitating the occurrence of the reaction and making the product more stable than the reactant. The use of the explicit solvent model and the selection of two CVs enabled the obtainment of a completely free energy landscape of PT and the characteristics of collective compression, which could not be achieved by previous static calculations.

3.4. Dehydration Reactions and Stability Evaluation. Herein, a total of twelve trajectories describing the evolution of $\text{Al}(\text{H}_2\text{O})_6^{3+}$ under varying local alkaline conditions are presented (Figure S4). All intermediate and final products that arise during the reaction process in these trajectories are

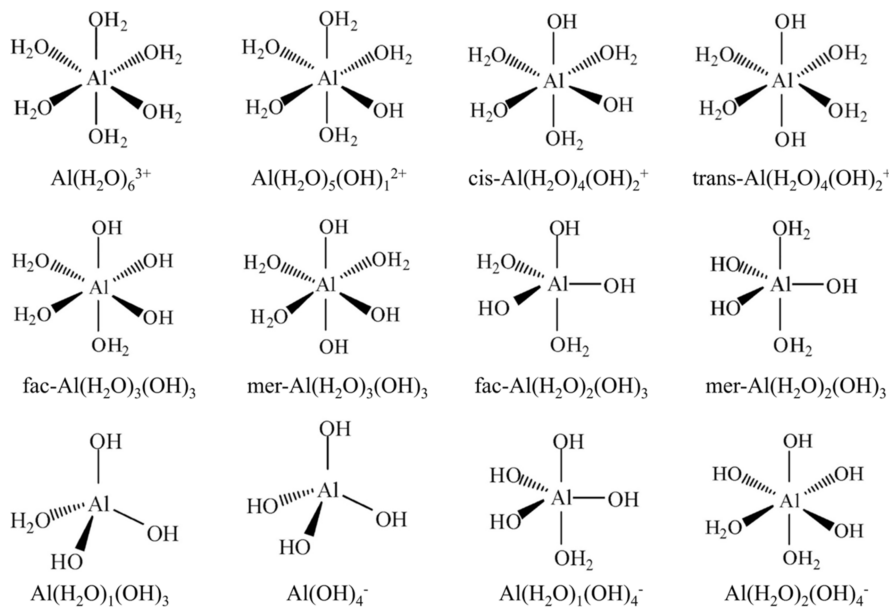


Figure 6. Schematic diagram for the configurations of aluminum monomers in AIMD simulations.

Table 2. Average Values of Topological Descriptors (All Units in au) and Mayer Bond Order Related to $\text{Al}-\text{O}_w$ Bonds in Various Configurations^a

configurations	ρ_{bcp}	$\nabla^2\rho_{\text{bcp}}$	$ V_{\text{bcp}} /G_{\text{bcp}}$	$H_{\text{bcp}} \times 10^4$	$ H_{\text{bcp}} /\rho_{\text{bcp}}$	Mayer bond order
$\text{Al}(\text{H}_2\text{O})_6^{3+}$	0.063	0.384	1.005	-4.76	-0.0075	0.640
$\text{Al}(\text{H}_2\text{O})_5(\text{OH})_1^{2+}$	0.057	0.342	0.992	4.84	0.0084	0.577
$\text{cis-Al}(\text{H}_2\text{O})_4(\text{OH})_2^+$	0.051	0.296	0.981	14.1	0.028	0.518
$\text{trans-Al}(\text{H}_2\text{O})_4(\text{OH})_2^+$	0.052	0.302	0.981	13.8	0.027	0.517
$\text{fac-Al}(\text{H}_2\text{O})_3(\text{OH})_3$	0.043	0.247	0.964	21.4	0.049	0.444
$\text{mer-Al}(\text{H}_2\text{O})_3(\text{OH})_3$	0.045	0.256	0.969	19.0	0.042	0.457
$\text{mer-Al}(\text{H}_2\text{O})_2(\text{OH})_3$	0.048	0.272	0.988	8.40	0.018	0.508
$\text{fac-Al}(\text{H}_2\text{O})_2(\text{OH})_3$						
(H_2O at AP)	0.045	0.246	0.987	7.79	0.017	0.484
$\text{fac-Al}(\text{H}_2\text{O})_2(\text{OH})_3$						
(H_2O at EP)	0.068	0.413	1.018	-19.3	-0.028	0.655
$\text{Al}(\text{H}_2\text{O})_1(\text{OH})_3$	0.066	0.402	1.004	-4.27	-0.0065	0.573

^aElectron density (ρ_{bcp}), Laplacian of the electron density ($\nabla^2\rho_{\text{bcp}}$), potential energy density (V_{bcp}), kinetic energy density (G_{bcp}), and energy density (H_{bcp}).

shown in Figure 6. The stability of these products in the solution system is determined by observing whether or not a dehydration reaction occurs. Considering the cost and reasonability of the calculation, one product is considered stable in solution if no dehydration reaction occurs within 25 ps AIMD.^{16,17} In the presence of one OH^- ion in solution, only one product, namely, $\text{Al}(\text{H}_2\text{O})_5(\text{OH})_1^{2+}$, is observed. This species is stable as no changes were observed during the following 25 ps of AIMD analysis. In the presence of two OH^- ions in solution, two isomers, $\text{cis-Al}(\text{H}_2\text{O})_4(\text{OH})_2^+$ and $\text{trans-Al}(\text{H}_2\text{O})_4(\text{OH})_2^+$, are generated after two stepwise PT events. Neither of these isomers undergoes dehydration reactions within 25 ps AIMD, suggesting their stability in the aqueous solution. With the presence of three OH^- ions, the $\text{Al}(\text{H}_2\text{O})_6^{3+}$ species converts to two isomers, $\text{mer-Al}(\text{H}_2\text{O})_3(\text{OH})_3$ and $\text{fac-Al}(\text{H}_2\text{O})_3(\text{OH})_3$, following three stepwise PT events. Both isomers undergo two stepwise dehydration reactions, ultimately resulting in the stable final product, $\text{Al}(\text{H}_2\text{O})_1(\text{OH})_3$, within the next 25 ps AIMD. Specifically, the existence time of the two isomers of $\text{Al}(\text{H}_2\text{O})_3(\text{OH})_3$ is less than 1 ps in AIMD trajectories, indicating that they are unstable and tend to

dehydrate. The dehydration reactions of $\text{fac-Al}(\text{H}_2\text{O})_2(\text{OH})_3$ in two independent trajectories occur at the apical position (AP). When four OH^- ions are present in the solution, only one final product, $\text{Al}(\text{OH})_4^-$, is observed, and it remains stable for the next 25 ps AIMD. However, after the intermediate product, $\text{Al}(\text{H}_2\text{O})_3(\text{OH})_3$ appears in each of the three trajectories following three stepwise PT events, the reaction order of subsequent hydrolysis and dehydration varies in the different trajectories, with some proceeding through a series of dehydration reactions prior to hydrolysis, while others undergo both dehydration and hydration reactions before ultimately undergoing hydrolysis. These results suggest that the order of hydrolysis and dehydration reactions is not fixed during the transformation of $\text{Al}(\text{H}_2\text{O})_3(\text{OH})_3$ to $\text{Al}(\text{OH})_4^-$. The occurrence of hydration reaction eq 7 in AIMD signifies that the conversion energy barrier between $\text{Al}(\text{H}_2\text{O})_1(\text{OH})_3$ and $\text{mer-Al}(\text{H}_2\text{O})_2(\text{OH})_3$ is not high under alkaline conditions. Notably, a recent study found that as the pH increases, the most stable state of aluminum monomers gradually changes from 6-fold coordinated $\text{Al}(\text{H}_2\text{O})_6^{3+}$ to 4-fold $\text{Al}(\text{OH})_4^-$, and different charge states $\text{Al}(\text{H}_2\text{O})_n(\text{OH})_m^{3-m}$ may coexist in

equilibrium.⁶¹ The assumption of stability of various hydrolysis products obtained from our AIMD simulations is consistent with the conclusions drawn from the umbrella sampling approach in the abovementioned study, as well as the dehydration-free energy data in previous static calculations.²⁶

3.5. Topological Analysis. To reveal the hidden reasons for the stability of aluminum monomers, these electronic structures were analyzed by means of topological analysis. The topological analysis in this work involved the determination of the complete topological descriptor values of BCPs in Al–O_w for the nine configurations under investigation. The corresponding configurations and topological descriptor values are supplemented in Figure S5 and Tables S2–S6, respectively. Table 2 lists the average descriptor values in each configuration except for *fac*-Al(H₂O)₂(OH)₃. Notably, while the descriptor values of different BCPs were evenly distributed in other configurations, in *fac*-Al(H₂O)₂(OH)₃, the two sets of values were significantly different. Consequently, we listed separately the values of BCPs involving equatorial position (EP) H₂O and AP H₂O. Meanwhile, the average Mayer bond order values of Al–O_w in the nine configurations were also determined, and the complete Mayer bond order values are supplemented in Tables S2–S6. Overall, the values of $\nabla^2\rho_{\text{bcp}}$ (all larger than 0), $|V_{\text{bcp}}|/G_{\text{bcp}}$ (around 1), and H_{bcp} (around 0) indicate that the coordination of Al³⁺ and H₂O is primarily involved in closed-shell interactions. Specifically, the $|V_{\text{bcp}}|/G_{\text{bcp}}$ values are slightly larger than 1, and H_{bcp} values are less than 0 in Al(H₂O)₆³⁺, *fac*-Al(H₂O)₂(OH)₃ (H₂O at AP), and Al(H₂O)₁(OH)₃, suggesting the weak covalent effects between aluminum and coordinated water.^{62,63} With the increase of OH ligand number from 0 to 3 in hexa-coordinated configurations, the values of ρ_{bcp} and Mayer bond order are decreased, and the values of $H_{\text{bcp}}/\rho_{\text{bcp}}$ are increased gradually, illustrative of the diminishment of the interaction between coordinated water molecules and the Al³⁺ ion along with the increase of OH ligands in hexa-coordinated configurations. Consistent with the preceding AIMD simulation results, the interaction is weak enough to induce dehydration reactions when three OH ligands are coordinated to Al³⁺. Notably, the values of ρ_{bcp} and Mayer bond order of Al–O_w at EP in *fac*-Al(H₂O)₂(OH)₃ are larger than those at AP, which demonstrates the stronger interaction at EP and also accounts for why the dehydration of *fac*-Al(H₂O)₂(OH)₃ in AIMD occurs at EP rather than AP.

4. CONCLUSIONS

In summary, we present a comprehensive analysis of the hydroxyl ion-induced hydrolysis of aluminum monomer under varying local alkaline conditions through AIMD. The reactions of Al(H₂O)_n(OH)_m^{3-m} with external OH⁻ exhibit three distinct PT pathways, namely, double jump mode, triple jump mode, and single jump mode. Specifically, the double jump mode is observed to be the most frequently occurring PT pathway in reactions involving OH⁻ and Al(H₂O)_n(OH)_m^{3-m} when $m < 3$. In contrast, a single jump mode tends to appear in cases where $n = 2$ or 3 for the configuration Al(H₂O)_n(OH)₃. Notably, the double and triple jump mode PT events are consistently accompanied by water wire compression. The free energy barrier associated with a double jump mode PT in the reaction of Al(H₂O)₆³⁺ and OH⁻ is found to be as low as 4 kJ mol⁻¹, with the free energy of the product approximately 40 kJ mol⁻¹ lower than that of the reactant. Consequently, the occurrence of double jump mode PT events in conjunction with water wire compression is highly plausible in hydroxyl

ion-induced hydrolysis. The hexa-coordinated configurations, namely, Al(H₂O)₆³⁺, Al(H₂O)₅(OH)₁²⁺, and Al(H₂O)₄(OH)₂⁺, are maintained in solution. Whereas the configuration Al(H₂O)₃(OH)₃ is exceedingly unstable and dehydration reactions readily transpire, the final dehydration product is recorded to be Al(H₂O)₁(OH)₃. In addition, the topological analysis reveals that the interaction between Al³⁺ and coordinated water weakens as the number of OH ligands increases from 0 to 3 in hexa-coordinated configurations, while it strengthens as the water ligand number n decreases from 3 to 1 in Al(H₂O)_n(OH)₃.

■ ASSOCIATED CONTENT

SI Supporting Information

The Supporting Information is available free of charge at <https://pubs.acs.org/doi/10.1021/acs.jpcb.3c02805>.

Details for the pre-equilibrium simulations, wall restraints in well-tempered metadynamics, condensed-to-atom electrophilicity index values, and results for topological analysis (PDF)

■ AUTHOR INFORMATION

Corresponding Authors

Yuguo Xia – National Engineering Research Center for Colloidal Materials, School of Chemistry and Chemical Engineering, Shandong University, 250100 Jinan, Shandong, China;  orcid.org/0000-0002-0405-3439; Email: xyg@sdu.edu.cn

Xiuling Jiao – National Engineering Research Center for Colloidal Materials, School of Chemistry and Chemical Engineering, Shandong University, 250100 Jinan, Shandong, China;  orcid.org/0000-0002-4358-7396; Email: jiaoxl@sdu.edu.cn

Authors

Longfei Guo – National Engineering Research Center for Colloidal Materials, School of Chemistry and Chemical Engineering, Shandong University, 250100 Jinan, Shandong, China

Dairong Chen – National Engineering Research Center for Colloidal Materials, School of Chemistry and Chemical Engineering, Shandong University, 250100 Jinan, Shandong, China;  orcid.org/0000-0001-6961-9328

Complete contact information is available at:

<https://pubs.acs.org/10.1021/acs.jpcb.3c02805>

Author Contributions

Y.X. supervised the project. L.G. performed all the simulations and elemental data analysis. X.J. and D.C. discussed the theoretical results and provided the fund support. L.G. and Y.X. wrote this manuscript, and all authors contributed to the overall scientific interpretation and revised this paper.

Notes

The authors declare no competing financial interest.

■ ACKNOWLEDGMENTS

This work was financially supported by the Young Scholars Program of Shandong University and the National Natural Science Foundation of China (grant 22275116). The authors acknowledge Beijing PARATERA Tech CO., Ltd., for providing HPC resources that have contributed to the research results reported in this paper.

■ REFERENCES

- (1) Chatterjee, M.; Naskar, M. K.; Chakrabarty, P. K.; Ganguli, D. Sol-gel alumina fibre mats for high-temperature applications. *Mater. Lett.* **2002**, *57*, 87–93.
- (2) Pauzi, M. Z. M.; Mahpoz, N. M. a.; Abdullah, N.; Rahman, M. A.; Abas, K. H.; Aziz, A. A.; Padzillah, M. H.; Othman, M. H. D.; Jaafar, J.; Ismail, A. F. Feasibility study of CAU-1 deposited on alumina hollow fiber for desalination applications. *Sep. Purif. Technol.* **2019**, *217*, 247–257.
- (3) Terra, N. M.; Lemos, C. O. T.; Silva, F. B. d.; Cardoso, V. L.; Reis, M. H. M. Characterisation of Asymmetric Alumina Hollow Fibres: Application for Hydrogen Permeation in Composite Membranes. *Braz. J. Chem. Eng.* **2016**, *33*, 567–576.
- (4) He, Z.; Lan, H.; Gong, W.; Liu, R.; Gao, Y.; Liu, H.; Qu, J. Coagulation behaviors of aluminum salts towards fluoride: Significance of aluminum speciation and transformation. *Sep. Purif. Technol.* **2016**, *165*, 137–144.
- (5) Wang, X.; Xu, H.; Wang, D. Mechanism of fluoride removal by AlCl_3 and Al_{13} : The role of aluminum speciation. *J. Hazard. Mater.* **2020**, *398*, 122987.
- (6) He, J.; Avnir, D.; Zhang, L. Sol-gel derived alumina glass: Mechanistic study of its structural evolution. *Acta Mater.* **2019**, *174*, 418–426.
- (7) Kobayashi, Y.; Yasuda, Y.; Morita, T. Low-temperature synthesis of α -alumina based on sol-gel processes. *Adv. Mater. Processes Technol.* **2020**, *7*, 482–513.
- (8) Zhang, H.; Zeng, D.; Wang, B.; Yang, J. Preparation and characteristics of spinnable sol and continuous mullite fibers with nano silica addition. *J. Sol. Gel Sci. Technol.* **2013**, *69*, 311–319.
- (9) Cividanes, L. S.; Campos, T. M. B.; Rodrigues, L. A.; Brunelli, D. D.; Thim, G. P. Review of mullite synthesis routes by sol-gel method. *J. Sol. Gel Sci. Technol.* **2010**, *55*, 111–125.
- (10) Li, L.; Liu, X.; Wang, G.; Liu, Y.; Kang, W.; Deng, N.; Zhuang, X.; Zhou, X. Research progress of ultrafine alumina fiber prepared by sol-gel method: A review. *Chem. Eng. J.* **2021**, *421*, 127744.
- (11) Ye, C.; Bi, Z.; Wang, D. Formation of Al_{30} from aqueous polyaluminum chloride under high temperature: Role of Al_{13} aggregates. *Colloids Surf., A* **2013**, *436*, 782–786.
- (12) Jolivet, J.-P.; Chanéac, C.; Chiche, D.; Cassaignon, S.; Durupthy, O.; Hernandez, J. Basic concepts of the crystallization from aqueous solutions: The example of aluminum oxy(hydroxi)des and aluminosilicates. *Compt. Rendus Geosci.* **2011**, *343*, 113–122.
- (13) Cardona, Y.; Korili, S. A.; Gil, A. Understanding the formation of Al_{13} and Al_{30} polycations to the development of microporous materials based on Al_{13} -and Al_{30} -PILC montmorillonites: a review. *Appl. Clay Sci.* **2021**, *203*, 105996.
- (14) Kabelitz, A.; Dinh, H. A.; Emmerling, F. Early stage in situ detection of polynuclear aluminum phases in aqueous solution. *Polyhedron* **2019**, *170*, 639–648.
- (15) Pouvreau, M.; Martinez-Baez, E.; Dembowski, M.; Pearce, C. I.; Schenter, G. K.; Rosso, K. M.; Clark, A. E. Mechanisms of Al^{3+} Dimerization in Alkaline Solutions. *Inorg. Chem.* **2020**, *59*, 18181–18189.
- (16) Lanzani, G.; Seitsonen, A. P.; Iannuzzi, M.; Laasonen, K.; Pehkonen, S. O. Isomerism of Trimeric Aluminum Complexes in Aqueous Environments: Exploration via DFT-Based Metadynamics Simulation. *J. Phys. Chem. B* **2016**, *120*, 11800–11809.
- (17) Giacobello, F.; Mollica-Nardo, V.; Foti, C.; Ponterio, R. C.; Saija, F.; Trusso, S.; Sponer, J.; Cassone, G.; Giuffrè, O. Hydrolysis of Al^{3+} in Aqueous Solutions: Experiments and Ab Initio Simulations. *Liquids* **2022**, *2*, 26–38.
- (18) Jin, X.; Liao, R.; Zhang, T.; Li, H. Theoretical insights into the dimerization mechanism of aluminum species at two different pH conditions. *Inorg. Chim. Acta* **2021**, *520*, 120311.
- (19) Cauet, E.; Bogatko, S.; Weare, J. H.; Fulton, J. L.; Schenter, G. K.; Bylaska, E. J. Structure and dynamics of the hydration shells of the Zn^{2+} ion from ab initio molecular dynamics and combined ab initio and classical molecular dynamics simulations. *J. Chem. Phys.* **2010**, *132*, 194502.
- (20) Persson, I. Structures of Hydrated Metal Ions in Solid State and Aqueous Solution. *Liquids* **2022**, *2*, 210–242.
- (21) Ikeda, T.; Hirata, M.; Kimura, T. Ab initio molecular dynamics study of polarization effects on Ionic Hydration in aqueous AlCl_3 solution. *J. Chem. Phys.* **2003**, *119*, 12386–12392.
- (22) Boekell, N. G.; Flowers, R. A. Coordination-Induced Bond Weakening. *Chem. Rev.* **2022**, *122*, 13447–13477.
- (23) Dong, S.; Shi, W.; Zhang, J.; Bi, S. DFT Studies on the Water-Assisted Synergistic Proton Dissociation Mechanism for the Spontaneous Hydrolysis Reaction of Al^{3+} in Aqueous Solution. *ACS Earth Space Chem.* **2018**, *2*, 269–277.
- (24) Dong, S.; Shi, W.; Zhang, J.; Bi, S. Density functional theory studies on the external OH^- -induced barrierless proton dissociation mechanism for the forced hydrolysis reaction of Al^{3+} (aq). *Int. J. Quantum Chem.* **2018**, *118*, No. e25682.
- (25) Dong, S.; Zhang, J.; Yuan, X.; Bi, S. Density Functional Theory Studies on the Real and Apparent Water-Exchange Reaction Kinetics of Al^{3+} in Aqueous Solution. *ACS Earth Space Chem.* **2019**, *3*, 2315–2322.
- (26) Dong, S.; Shi, W.; Zhang, J.; Bi, S. ^{27}Al NMR Chemical Shifts and Relative Stabilities of Aqueous Monomeric Al^{3+} Hydrolytic Species with Different Coordination Structures. *ACS Earth Space Chem.* **2019**, *3*, 1353–1361.
- (27) Truhlar, D. G. Ab Initio Molecular Dynamics: Basic Theory and Advanced Methods. *Phys. Today* **2010**, *63*, 54–56.
- (28) VandeVondele, J.; Krack, M.; Mohamed, F.; Parrinello, M.; Chassaing, T.; Hutter, J. Quickstep: Fast and accurate density functional calculations using a mixed Gaussian and plane waves approach. *Comput. Phys. Commun.* **2005**, *167*, 103–128.
- (29) Kuhne, T. D.; Iannuzzi, M.; Del Ben, M.; Rybkin, V. V.; Seewald, P.; Stein, F.; Laino, T.; Khalil, R. Z.; Schutt, O.; Schiffmann, F.; Golze, D.; Wilhelm, J.; Chulkov, S.; Bani-Hashemian, M. H.; Weber, V.; Borstnik, U.; Taillefumier, M.; Jakobovits, A. S.; Lazzaro, A.; Pabst, H.; Muller, T.; Schade, R.; Guidon, M.; Andermatt, S.; Holmberg, N.; Schenter, G. K.; Hehn, A.; Bussy, A.; Belleflamme, F.; Tabacchi, G.; Glööb, A.; Lass, M.; Bethune, I.; Mundy, C. J.; Plessl, C.; Watkins, M.; VandeVondele, J.; Krack, M.; Hutter, J. CP2K: An electronic structure and molecular dynamics software package - Quickstep: Efficient and accurate electronic structure calculations. *J. Chem. Phys.* **2020**, *152*, 194103.
- (30) Becke, A. D. Density-functional exchange-energy approximation with correct asymptotic behavior. *Phys. Rev. A* **1988**, *38*, 3098–3100.
- (31) Lee, C.; Yang, W.; Parr, R. G. Development of the Colle-Salvetti correlation-energy formula into a functional of the electron density. *Phys. Rev. B: Condens. Matter Mater. Phys.* **1988**, *37*, 785–789.
- (32) Grimme, S.; Antony, J.; Ehrlich, S.; Krieg, H. A consistent and accurate ab initio parametrization of density functional dispersion correction (DFT-D) for the 94 elements H-Pu. *J. Chem. Phys.* **2010**, *132*, 154104.
- (33) Wang, J.; Roman-Perez, G.; Soler, J. M.; Artacho, E.; Fernandez-Serra, M. V. Density, structure, and dynamics of water: the effect of van der Waals interactions. *J. Chem. Phys.* **2011**, *134*, 024516.
- (34) Gillan, M. J.; Alfe, D.; Michaelides, A. Perspective: How good is DFT for water? *J. Chem. Phys.* **2016**, *144*, 130901.
- (35) Lanzani, G.; Sarpola, A.; Saukkoriipi, J.; Laasonen, K.; Morrison, C. A.; Slater, B.; Rämö, J.; Pehkonen, S. O. Study of the stability of aluminium trimeric clusters in aqueous solutions. *Mol. Simul.* **2012**, *38*, 934–943.
- (36) Goedecker, S.; Teter, M.; Hutter, J. Separable Dual-Space Gaussian Pseudopotentials. *Phys. Rev. B: Condens. Matter Mater. Phys.* **1996**, *54*, 1703–1710.
- (37) Lippert, G.; Hutter, J.; Parrinello, M. A hybrid Gaussian and plane wave density functional scheme. *Mol. Phys.* **1997**, *92*, 477–487.
- (38) VandeVondele, J.; Hutter, J. Gaussian basis sets for accurate calculations on molecular systems in gas and condensed phases. *J. Chem. Phys.* **2007**, *127*, 114105.

- (39) Nosé, S. A unified formulation of the constant temperature molecular dynamics methods. *J. Chem. Phys.* **1984**, *81*, 511–519.
- (40) Hoover, W. G. Canonical dynamics: Equilibrium phase-space distributions. *Phys. Rev. A* **1985**, *31*, 1695–1697.
- (41) Brehm, M.; Thomas, M.; Gehrke, S.; Kirchner, B. TRAVIS-A free analyzer for trajectories from molecular simulation. *J. Chem. Phys.* **2020**, *152*, 164105.
- (42) Chen, M.; Zheng, L.; Santra, B.; Ko, H. Y.; DiStasio Jr, R. A.; Klein, M. L.; Car, R.; Wu, X. Hydroxide diffuses slower than hydronium in water because its solvated structure inhibits correlated proton transfer. *Nat. Chem.* **2018**, *10*, 413–419.
- (43) Laio, A.; Parrinello, M. Escaping free-energy minima. *Proc. Natl. Acad. Sci. U.S.A.* **2002**, *99*, 12562–12566.
- (44) Barducci, A.; Bussi, G.; Parrinello, M. Well-tempered metadynamics: a smoothly converging and tunable free-energy method. *Phys. Rev. Lett.* **2008**, *100*, 020603.
- (45) Tribello, G. A.; Bonomi, M.; Branduardi, D.; Camilloni, C.; Bussi, G. PLUMED 2: New feathers for an old bird. *Comput. Phys. Commun.* **2014**, *185*, 604–613.
- (46) Trapl, D.; Spiwok, V. Analysis of the Results of Metadynamics Simulations by metadynminer and metadynminer3d. *R Journal* **2022**, *14*, 46–58.
- (47) Frisch, M. J.; Trucks, G. W.; Schlegel, H. B.; Scuseria, G. E.; Robb, M. A.; Cheeseman, J. R.; Scalmani, G.; Barone, V.; Mennucci, B.; Petersson, G. A.; Nakatsuji, H.; Caricato, M.; Li, X.; Hratchian, H. P.; Izmaylov, A. F.; Bloino, J.; Zheng, G.; Sonnenberg, J. L.; Hada, M.; Ehara, M.; Toyota, K.; Fukuda, R.; Hasegawa, J.; Ishida, M.; Nakajima, T.; Honda, Y.; Kitao, O.; Nakai, H.; Vreven, T.; Montgomery, J. A., Jr.; Peralta, J. E.; Ogliaro, F.; Bearpark, M.; Heyd, J. J.; Brothers, E.; Kudin, K. N.; Staroverov, V. N.; Kobayashi, R.; Normand, J.; Raghavachari, K.; Rendell, A.; Burant, J. C.; Iyengar, S. S.; Tomasi, J.; Cossi, M.; Rega, N.; Millam, N. J.; Klene, M.; Knox, J. E.; Cross, J. B.; Bakken, V.; Adamo, C.; Jaramillo, J.; Gomperts, R.; Stratmann, R. E.; Yazyev, O.; Austin, A. J.; Cammi, R.; Pomelli, C.; Ochterski, J. W.; Martin, R. L.; Morokuma, K.; Zakrzewski, V. G.; Voth, G. A.; Salvador, P.; Dannenberg, J. J.; Dapprich, S.; Daniels, A. D.; Farkas, O.; Foresman, J. B.; Ortiz, J. V.; Cioslowski, J.; Fox, D. J. *Gaussian 09*. Revision B.01; Gaussian, Inc.: Wallingford, CT, 2010;
- (48) Cancès, E.; Mennucci, B.; Tomasi, J. A new integral equation formalism for the polarizable continuum model: Theoretical background and applications to isotropic and anisotropic dielectrics. *J. Chem. Phys.* **1997**, *107*, 3032–3041.
- (49) Bader, R. F. W. *Atoms In Molecules*; Clarendon Press, 1990.
- (50) Bridgeman, A. J.; Caviglasso, G.; Ireland, L. R.; Rothery, J. The Mayer bond order as a tool in inorganic chemistry†. *Dalton Trans.* **2001**, *14*, 2095–2108.
- (51) Lu, T.; Chen, F. Multiwfns: a multifunctional wavefunction analyzer. *J. Comput. Chem.* **2012**, *33*, 580–592.
- (52) Smirnov, P. R.; Grechin, O. V. Structure of the Nearest Environment of Ions in Aqueous Solutions of Aluminum Chloride According to X-ray Diffraction. *Russ. J. Inorg. Chem.* **2018**, *63*, 1251–1255.
- (53) Hassanali, A.; Prakash, M. K.; Eshet, H.; Parrinello, M. On the recombination of hydronium and hydroxide ions in water. *Proc. Natl. Acad. Sci. U.S.A.* **2011**, *108*, 20410–20415.
- (54) Hassanali, A.; Giberti, F.; Cuny, J.; Kuhne, T. D.; Parrinello, M. Proton transfer through the water gossamer. *Proc. Natl. Acad. Sci. U.S.A.* **2013**, *110*, 13723–13728.
- (55) Tuckerman, M. E.; Marx, D.; Parrinello, M. The nature and transport mechanism of hydrated hydroxide ions in aqueous solution. *Nature* **2002**, *417*, 925–929.
- (56) Tuckerman, M. E.; Chandra, A.; Marx, D. Structure and Dynamics of OH[−](aq). *Acc. Chem. Res.* **2006**, *39*, 151–158.
- (57) Marx, D.; Chandra, A.; Tuckerman, M. E. Aqueous basic solutions: Hydroxide solvation, structural diffusion, and comparison to the hydrated Proton. *Chem. Rev.* **2010**, *110*, 2174–2216.
- (58) Putz, M.; Mingos, D. *Applications of Density Functional Theory to Chemical Reactivity. Structure and Bonding*; Springer: Berlin Heidelberg, 2013.
- (59) Parr, R. G.; Szentpály, L. v.; Liu, S. Electrophilicity index. *J. Am. Chem. Soc.* **1999**, *121*, 1922–1924.
- (60) Esmaeilbeig, M. A.; Khorram, M.; Ayatollahi, S.; Zolghadr, A. R. On the hydrolysis of iron ions: DFT-based molecular dynamics perspective. *J. Mol. Liq.* **2022**, *367*, 120323.
- (61) Legg, B. A.; Baer, M. D.; Chun, J.; Schenter, G. K.; Huang, S.; Zhang, Y.; Min, Y.; Mundy, C. J.; De Yoreo, J. J. Visualization of Aluminum Ions at the Mica Water Interface Links Hydrolysis State-to-Surface Potential and Particle Adhesion. *J. Am. Chem. Soc.* **2020**, *142*, 6093–6102.
- (62) Cremer, D.; Kraka, E. Chemical Bonds without Bonding Electron Density? Does the Difference Electron-Density Analysis Suffice for a Description of the Chemical Bond? *Angew. Chem., Int. Ed.* **1984**, *23*, 627–628.
- (63) Bianchi, R.; Gervasio, G.; Marabello, D. Experimental Electron Density Analysis of Mn₂(Co)₁₀: metal-metal and metal-ligand bond characterization. *Inorg. Chem.* **2000**, *39*, 2360–2366.